Nanowire Structural Evolution from Fe_3O_4 to ε-Fe_2O_3**

By *Yong Ding*, *Jenny Ruth Morber*, *Robert L. Snyder*,* and *Zhong Lin Wang**

The ε-Fe_2O_3 phase is commonly considered an intermediate phase during thermal treatment of maghemite (γ-Fe_2O_3) to hematite (α-Fe_2O_3). The routine method of synthesis for ε-Fe_2O_3 crystals uses γ-Fe_2O_3 as the source material and requires dispersion of γ-Fe_2O_3 into silica, and the obtained ε-Fe_2O_3 particle size is rather limited, typically under 200 nm. In this paper, by using a pulsed laser deposition method and Fe_3O_4 powder as a source material, the synthesis of not only one-dimensional Fe_3O_4 nanowires but also high-yield ε-Fe_2O_3 nanowires is reported for the first time. A detailed transmission electron microscopy (TEM) study shows that the nanowires of pure magnetite grow along [111] and <211> directions, although some stacking faults and twins exist. However, magnetite nanowires growing along the <110> direction are found in every instance to accompany a new phase, ε-Fe_2O_3, with some micrometer-sized wires even fully transferring to ε-Fe_2O_3 along the fixed structural orientation relationship, $(001)_{\varepsilon\text{-}Fe_2O_3}\|(111)_{Fe_3O_4}$, $[010]_{\varepsilon\text{-}Fe_2O_3}\|<110>_{Fe_3O_4}$. Contrary to generally accepted ideas regarding epsilon phase formation, there is no indication of γ-Fe_2O_3 formation during the synthesis process; the phase transition may be described as being from Fe_3O_4 to ε-Fe_2O_3, then to α-Fe_2O_3. The detailed structural evolution process has been revealed by using TEM. 120° rotation domain boundaries and antiphase boundaries are also frequently observed in the ε-Fe_2O_3 nanowires. The observed ε-Fe_2O_3 is fundamentally important for understanding the magnetic properties of the nanowires.

1. Introduction

Among the polymorphs of ferric oxides, maghemite (γ-Fe_2O_3) and hematite (α-Fe_2O_3) are well known,[1–5] however, knowledge of ε-Fe_2O_3, considered an intermediate phase between maghemite and hematite, is relatively limited. The disparity is most likely due to difficulties in stabilizing the ε-Fe_2O_3 phase. The earliest known report on the existence of ε-Fe_2O_3 was published in 1934 by Forestier and Guillain.[6] However, detailed structural characterization of this phase was not published until 1998 by Tronc et al.,[7] and was later refined in 2005 by Kelm and Mader.[8] Zboril et al. observed the transformation of γ-$Fe_2O_3 \rightarrow \varepsilon Fe_2O_3 \rightarrow \alpha$-$Fe_2O_3$ in small particles through using Mossbauer spectroscopy in 2002, noting that, most likely, the formation of ε-Fe_2O_3 as an intermediate was related to the degree of agglomeration in precursor powders, with those more loosely packed tending to form the intermediate, and those with heavy agglomeration tending to lead straight to the more stable alpha phase.[9] When considered in the framework of nanomaterials, this finding is interesting, perhaps indicating the role of high surface energy, a characteristic of most nanostructures, as a key component in the formation of the epsilon phase.

Until now, the γ-$Fe_2O_3 \rightarrow \varepsilon$-$Fe_2O_3 \rightarrow \alpha$-$Fe_2O_3$ pathway was the only known route to the synthesis of ε-Fe_2O_3, however, our work indicates a completely novel synthesis path, one involving magnetite (Fe_3O_4), rather than maghemite as the precursor phase. In hindsight, it is perhaps not surprising that if maghemite can give rise to the epsilon phase, magnetite can do so as well. Both magnetite and maghemite phases share the same basic structure, with close-packed oxygen atoms resting in an alternating ABCABC stacking sequence along the [111] direction, and Fe occupying octahedral or tetragonal lattice sites. The distinguishing feature of the gamma phase is that some Fe positions are left unoccupied as random vacancies, reducing the ordering in crystal structure. In transmission electron microscopy (TEM), this loss of symmetry corresponds to the appearance of diffraction spots that should be forbidden in a more perfect lattice. Most likely, previous observations of ε-Fe_2O_3 described the phase as an intermediate of γ-Fe_2O_3 and not Fe_3O_4 because of the additional complication of stoichiometry. The conversion from Fe_3O_4 to ε-Fe_2O_3 implies, equivalently, an overabundance of iron or an oxygen deficiency in the starting phase. Therefore, the forming material (ε-Fe_2O_3) must either get rid of the excess iron or adsorb additional oxygen atoms. For our high-surface-area nanowires grown via solid-state physical evaporation, oxygen adsorption would not be problematic. Likewise, at low pressures, it is possible that iron desorbed from the lattice. If oxygen had adsorbed into the lattice (or iron desorbed from the lattice) randomly, such that Fe site occupation was no longer periodic, the maghemite phase would have been observed. Our investigation shows a direct transition from Fe_3O_4 to ε-Fe_2O_3 without evidence of other intermediate phases, indicating that the formation of the epsilon phase was accompanied by perfectly ordered species evolution.

[*] Prof. R. L. Snyder, Prof. Z. L. Wang, Dr. Y. Ding, J. R. Morber
School of Materials Science and Engineering
Georgia Institute of Technology
Atlanta, Georgia 30332-0245 (USA)
E-mail: bob.snyder@mse.gatech.edu; zhong.wang@mse.gatch.edu

A standard synthesis method for ε-Fe$_2$O$_3$ nanocrystals presented in the literature is the heat treatment of γ-Fe$_2$O$_3$ nanoparticles dispersed in silica xerogels.[7,10–12] Drawbacks of this method include the existence of silica impurities and small grain size, which normally falls under 200 nm. For many potential applications, pure crystals of ε-Fe$_2$O$_3$ are required. Impurities can alter the performance of devices based on ε-Fe$_2$O$_3$ materials, and create obstacles in further refining or treatment. In addition, small particle sizes severely limit the applicability of these materials owing, in part, to practical complications regarding maneuverability and processing, as well as integration into larger systems. Other reported synthesis methods such as thermal decomposition, and previously reported high-energy deposition syntheses likewise produced products of mixed phase or other impurities, and often with low yield.[12] It is likely for these reasons that ε-Fe$_2$O$_3$ has not been more fully exploited in novel technologies.

Pure iron oxides, including maghemite and magnetite, have been widely used in many fields, from magnetic recording, storage, and magnetizable printing[13] to medical applications, such as cell separation and magnetic resonance imaging.[14] For future technological advances, further improvements of their magnetic properties are necessary.[15,16] While many applications require soft magnetic properties, large coercivities are required in applications such as high-density magnetic recording, where the magnetic domain needs to be stable, and desire for ever-smaller pixel sizes has pushed some traditional materials to the superparamagnetic limit. Researchers are currently working to maximize the coercivity in materials employed in these technologies. Ferric oxides like magnetite and maghemite are attractive choices for several reasons, including their low toxicity, low cost, availability, stability, high corrosion resistance, and high resistivity, which correlates to low eddy current energy loss.[17] However, their face-centered cubic crystal structure leads to a low magnetocrystalline anisotropy constant, therefore, augmentation of the coercive field (H_c) is difficult. Remarkably, the ε-Fe$_2$O$_3$ phase takes the orthorhombic crystal structure, producing a room-temperature H_c as large as 20 kOe.[11] As a comparison, the highly anisotropic magnetoplumbite barium hexaferrite (BaFe$_{12}$O$_{19}$), commonly utilized for magnetic recording, can only produce a coercive field as large as about 7.5 kOe 1 Oe = (1000/(4π)) A m^{-1}).[18] In addition, this magnetic behavior is stable at elevated temperatures in the epsilon phase, which has a reported Curie temperature of ca. 510 K.[19] Crystals of ε-Fe$_2$O$_3$ larger in size, yet still retaining the favorable characteristics observed at the nanoscale would prove ideal candidates for almost any technology requiring hard magnetic materials, and could provide the additional benefits of low toxicity, high corrosion resistance, and so forth, inherent to ferric oxide materials. Furthermore, long nanowires of this material are ideal morphologies for many current and future electronic, storage, and printing technologies. With further understanding of the phase stability and exploring new synthesis methods, ε-Fe$_2$O$_3$ may pride a replacement for maghemite and magnetite in many of their current applications, as well as those of more complex and expensive hard magnetic materials.

In this work, applying a pulsed laser deposition (PLD) method and Fe$_3$O$_4$ powder as a precursor, we synthesized, for the first time, not only one-dimensional Fe$_3$O$_4$ nanowires, but also high-yield ε-Fe$_2$O$_3$ nanowires. Specifics regarding synthesis parameters, nanowire alignment, and magnetic properties of these materials, as well as brief structural characterization information have been presented elsewhere.[20] Here, we report a much deeper and more detailed description of the structural evolution of three iron oxide phases found to exist in nanowires grown by using this method. Our findings demonstrate both a novel practical synthesis route for ε-Fe$_2$O$_3$ and, through detailed TEM investigation involving high-resolution images, systematic diffraction, and simulated models, the complete structural evolution process as observed within the nanowires themselves. This study could lay the foundation for exploring the magnetic properties of ε-Fe$_2$O$_3$ nanowires.

## 2. Structure and Structural Evolution

The synthesized Fe$_3$O$_4$ nanowires can be classified according to growth direction into three categories, as those growing along the $[111]_M$, the $[211]_M$, and the $[110]_M$ directions, which are displayed separately in Figures 1–3, respectively. (Note our notation convention of using M, ε, and H subscripts to denote the plane and orientation indices in Fe$_3$O$_4$ (magnetite), ε-Fe$_2$O$_3$, and α-Fe$_2$O$_3$ (hematite) phases, respectively. Also, though many of our examples appear to posses rectangular geometries, for simplicity, we will refer to all examined structures using the term "nanowire." Figure 1a and b shows the brightfield and dark-field TEM images of a Fe$_3$O$_4$ nanowire grown along the $[111]_M$ direction. The select-area electron diffraction (SAED) pattern in Figure 1c can be uniquely indexed using cubic-phase magnetite. Although some stacking faults can be
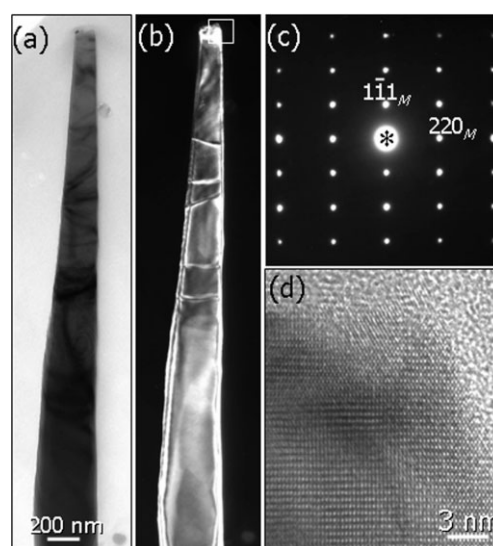
Figure 1. General morphology of the nanowires. TEM a) bright-field and b) dark-field images of the [111] growth magnetite nanowire. c) SAED pattern of the wire. d) HRTEM image recorded from the white rectangular area in (b).

identified in the dark-field image in Figure 1b, the entire wire is single crystalline and is well described as a pure magnetite structure. The high-resolution TEM (HRTEM) image in Figure 1d confirms the $[111]_M$ growth direction of the nanowire.

The nanowire displayed in Figure 2a takes the $<211>_M$ growth direction. Twin boundaries and stacking faults can be seen in the image. Further, the existence of twin structures also can be seen in the SAED pattern in Figure 2b. Without exception, all diffraction spots in Figure 2b can be indexed using the
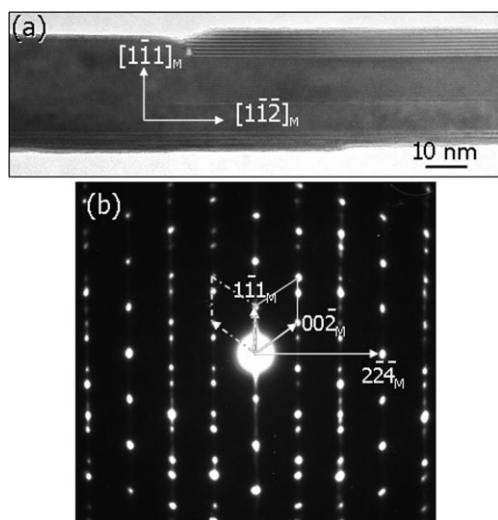
Figure 2. a) HRTEM image and b) SAED pattern of a magnetite nanowire grown along the <211> direction. Stacking faults and (111) twins can be observed in the HRTEM image.

twinned magnetite structure, taking $(111)_M$ as the twin plane. Although the planar defects exist within the wire, it is still best described as a phase of pure magnetite.

While the nanowire shown in Figure 3a grew along the $[110]_M$ direction, there are extra diffraction spots in the SAED pattern recorded from the whole nanowire, as shown in Figure 3b, which could not be fully indexed by the magnetite phase. Changing to a small select-area aperture, we created the SAED patterns shown in Figure 3c and d, recorded from the
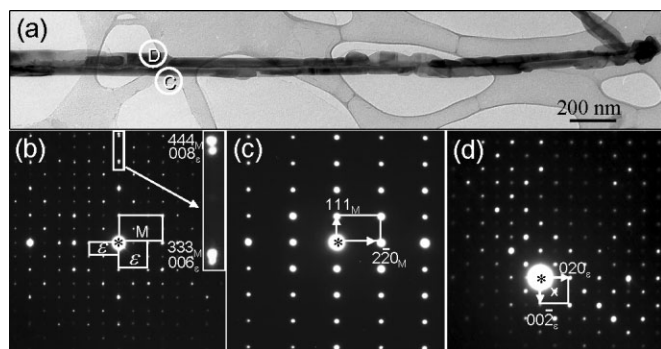
Figure 3. a) Low-magnification TEM image of a [110] growth magnetite nanowire. The SAED patterns from the whole wire, and circled areas "C" and "D" are displayed in (b), (c), and (d), respectively.

circled areas "C" and "D" in Figure 3a. The pattern in Figure 3c can be indexed as the lattice projection expected when the electron beam is parallel to $[\bar{1}\bar{1}2]_M$, while the SAED pattern in Figure 3d is indexed as the projected ε-Fe₂O₃ structure with the electron beam along $[100]_ε$. In order to confirm and clarify the presence of the ε-Fe₂O₃ phase, a systematic procedure involving construction of the lattice based on varying geometric projections observed in electron-diffraction patterns was used. Based on the series of electron-diffraction patterns shown in Figure 4, in which the sample was rotated along a fixed axis so that the electron beam would project atomic positions at known angles, we reconstructed the reciprocal space lattice shown in Figure 4f. Each diffraction pattern in Figure 4a–e cor-
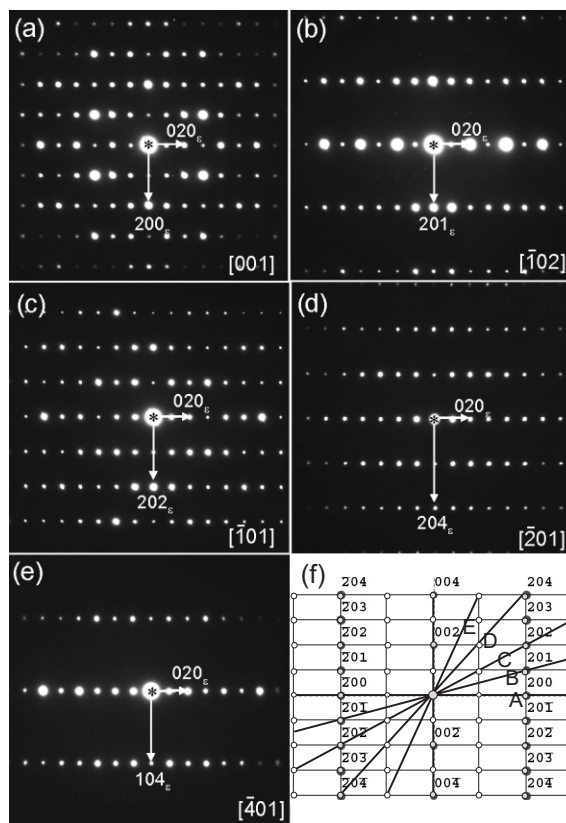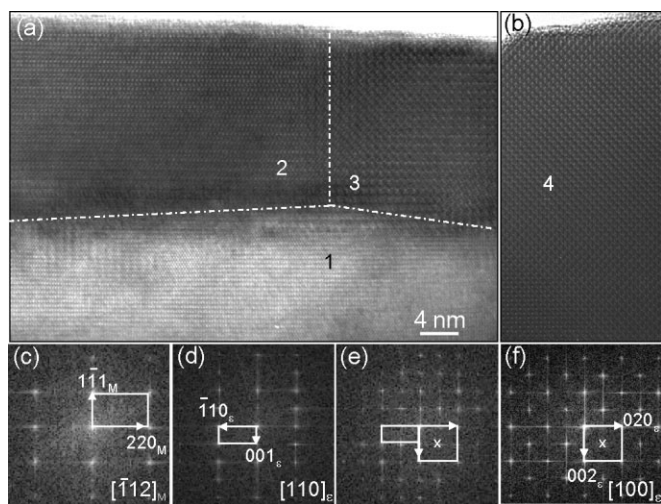

Figure 4. Multiple directional examination of the diffraction behavior of the ε-Fe₂O₃ nanowires. a–e) A series of zone-axis diffraction patterns of the ε-Fe₂O₃ phased wire with beam directions along the [001], [$\bar{1}$02] [$\bar{1}$01], [$\bar{2}$01], and [–401] directions, respectively. These diffraction patterns provide a systematic expression about the 3D structure of the ε-Fe₂O₃ phase. f) Schematic of the reciprocal space lattice built up from these patterns, where the reciprocal planes corresponding to the patterns displayed in (A–E) are marked.

responds to a slice through this reciprocal lattice at a unique orientation, identified by the matching letter label. This reciprocal space lattice was found to correspond to a real-space orthorhombic unit cell, with $a \sim 5.11$ Å, $b \sim 8.72$ Å, and $c \sim 9.42$ Å, parameters which match well to the ε-Fe₂O₃ phase.[7,8] Looking back to the SAED pattern in Figure 3b, the $(333)_M$ and $(444)_M$ diffraction spots are not single points, but

are separated into pairs, with the additional spots corresponding to $(006)_\varepsilon$ and $(008)_{\varepsilon''}$, as shown in the inset. This effect is due to the small difference between the planar distance of magnetite (111) and ε-Fe_2O_3 (001). There is no splitting of the $(333)_M$ and $(444)_M$ diffraction spots in Figures 1c and 2b, indicating the absence of the ε-Fe_2O_3 phase in these nanowires. Besides the $[\bar{1}\bar{1}2]_M$ pattern, two sets of ε-Fe_2O_3 patterns can be distinguished in Figure 3b. The structural relationship between magnetite and the ε-Fe_2O_3 phase can be described as, 1) $(001)_\varepsilon \| (111)_M$, $[010]_\varepsilon \| <110>_M$, and 2) $(001)_\varepsilon \| (111)_M$, $[1\bar{1}0]_\varepsilon \| <110>_M$. The two different structural relationships are due to the existence of 120° rotation domains in the ε-Fe_2O_3 section, which will be discussed later.
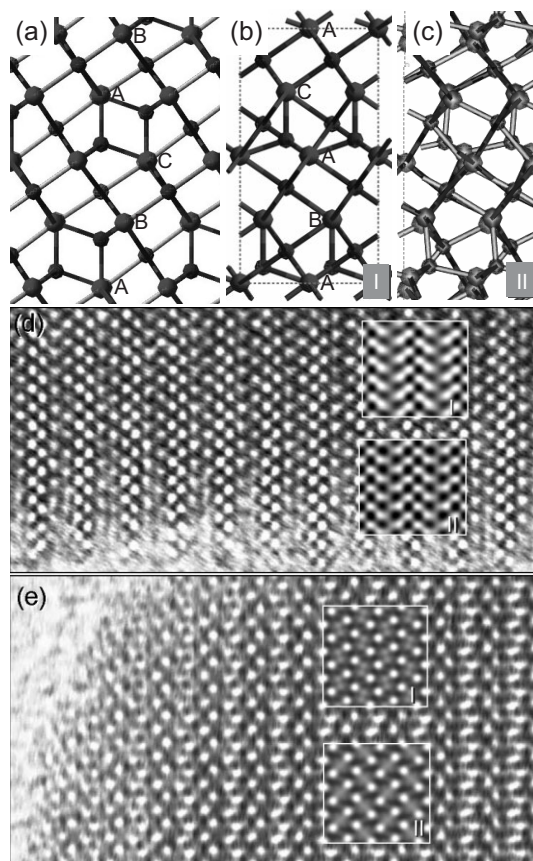
The HRTEM images in Figure 5a and b were recorded from the nanowire previously shown in Figure 3a. The fast Fourier transforms (FFT) from areas 1, 2, 3, and 4 are displayed in Figure 5c–f, respectively. After indexing these FFT patterns, we

Figure 6. Atomic models of a) magnetite, b) ε-Fe_2O_3 [7], and c) ε-Fe_2O_3 [8]. d,e) Experimental and simulated (inset) HRTEM images of the ε-Fe_2O_3 phase with the beam along the $[\bar{1}01]$ and $[001]$ directions, respectively. The insets are the simulated images based on model I and model II as displayed in (b) and (c), respectively, for the ε-Fe_2O_3 phase.

Figure 5. Domain structure in a single nanowire. a,b) HRTEM images recorded from the wire shown in Figure 3a. c–f) FFT patterns from the 1–4 areas shown in (a) and (b).

can find that area one corresponds to the magnetite phase, while areas two and four correspond to the ε-Fe_2O_3 phase, and area three is best described by two ε-Fe_2O_3 phase domains overlapped. The two individual structural relationships between magnetite and the ε-Fe_2O_3 phase can be confirmed in the HRTEM images.

From a crystallographic point of view, both magnetite and ε-Fe_2O_3 are composed of close-packed oxygen layers with Fe ions occupying the interstitial oxygen octahedral or tetragonal sites.[7,8,21,22] The close-packed oxygen layers in magnetite stack in a ...ABCABC... sequence along the $[111]_M$ direction, whereas the stacking sequence in ε-Fe_2O_3 changes to ...ABACABAC... along the $[001]_\varepsilon$ direction. Figure 6a shows a schematic ball-and-stick model of the magnetite structure, and Figure 6b and c shows similar models for the ε-Fe_2O_3 phase. In the two ε-Fe_2O_3 models, I and II in Figure 6, are based on the two structural characterizations reported in the literature;[7,8] model I is the ideal structure, whereas II is the refined struc-

ture. By tilting the nanowire, HRTEM images with the electron beam along the $[\bar{1}01]_\varepsilon$ and $[001]_\varepsilon$ directions were recorded in Figure 6d and e, respectively. Taking into account a sample thickness of 3.6 nm and Scherzer defocus effects, simulated images based on models I and II were created. The simulated patterns are seen in the small squares superimposed on the actual high-resolution images shown in Figure 6d and e. Comparing the two sets of simulated images, model II demonstrates a better match with the experimental data in both cases.

According to the literature, it is generally accepted that ε-Fe_2O_3 is well described as an intermediate phase between γ-Fe_2O_3 and a-Fe_2O_3.[7] In our experiment, we found that magnetite and ε-Fe_2O_3 phases coexist in our nanowires without the presence of γ-Fe_2O_3. It is therefore worthwhile to clarify the phase-transition process during the synthesis. It seems that the images in Figure 7 of a long wire and its SAED patterns seen in Figure 8 provide some hints regarding this issue. The existence of the Au catalyst at the tip of the wire suggests that the synthesis process follows the vapor–liquid–solid growth mechanism.[23] Figure 7a and b shows low-magnification TEM images from two connected parts of the same nanowire. The SAED patterns in Figure 8a–e are recorded from the circled areas "A"–"E" in Figure 7. The SAED pattern in Figure 8a shows
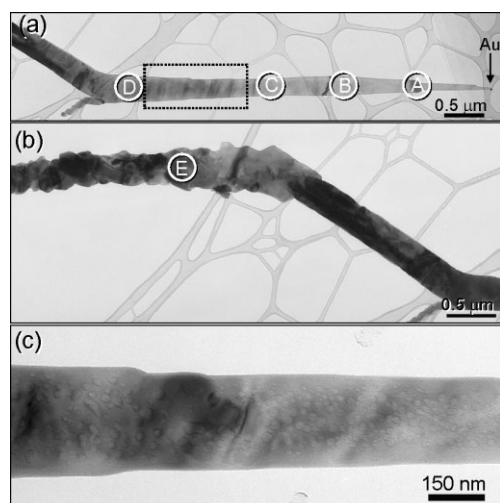
Figure 7. Structural evolution among the three phases along a single nanowire. a,b) Low-magnification TEM images showing different parts of the same nanowire. c) Enlarged image of the enclosed rectangular area in (a).
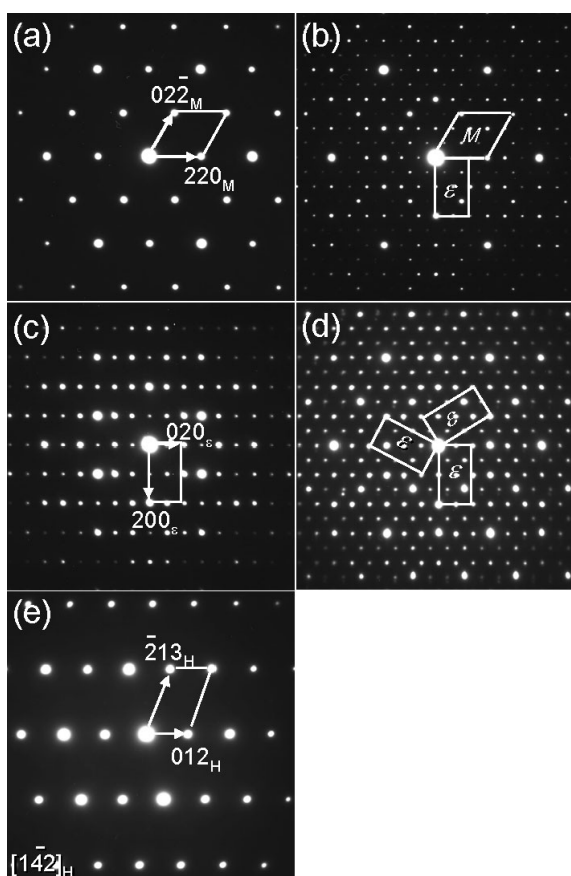

Figure 8. a–e) SAED patterns recorded from the circled areas A–E for the same nanowire presented in Figure 7, showing the different phases along the length of the same nanowire.

that area "A" close to the Au catalyst is composed of the pure magnetite phase. Area "B" is composed of two phases, magnetite and ε-Fe$_2$O$_3$, with a fixed orientation relationship between

them. Based on the SAED pattern shown in Figure 8b, this orientation relationship can be described as $(001)_ε \| (111)_M$, $[010]_ε \| <110>_M$, which is the same as that shown in Figure 3. Progressing to area "C", the nanowire here fully changes to the ε-Fe$_2$O$_3$ phase. At area "D", the diffraction pattern in Figure 8d is composed of three $[001]_ε$ patterns. By rotating 120° clockwise or anticlockwise around the $[001]_ε$ axis, each of these $[001]_ε$ patterns can be superimposed onto any of the other two $[001]_ε$ patterns. Relating this diffraction phenomenon back to a real-space structure, the diffraction pattern in Figure 8d signifies the formation of rotation domains, discussed later in more detail. There is some misalignment between the structure in areas "E" and in "A"–"D". We have to tilt the wire to get the right zone-axis SAED pattern, as shown in Figure 8e. Neither magnetite nor the ε-Fe$_2$O$_3$ phase can be used to index the pattern displayed in Figure 8e. Indeed, it belongs to the hematite phase, with the electron beam along the $[1\bar{4}2]_H$ direction. Although we cannot find the orientation relationship between the connected ε-Fe$_2$O$_3$ and α-Fe$_2$O$_3$ regions owing to the wire bending, the confirmation of the existence of the α-Fe$_2$O$_3$ phase is sufficient to understand the phase-transition process. In summary, the phase structure from the tip to the end of the nanowire changes continuously, from magnetite to ε-Fe$_2$O$_3$, then to α-Fe$_2$O$_3$. There is no evidence of the γ-Fe$_2$O$_3$ phase at any point.[24] If it did exist, the diffraction pattern could unambiguously separate it from the above three phases. Keeping in mind that the earliest formed portion of the wire should be the furthest away from the catalyst, with the latter or freshest growth occurring closest to the catalyst, we can assume that the as-deposited nanowires form the magnetite phase, and with time, oxidize into ε-Fe$_2$O$_3$, and later into α-Fe$_2$O$_3$. Figure 7c provides an enlarged image of the rectangular-enclosed area in Figure 7a. The bubblelike contrast in the TEM image might be regarded as evidence of oxidization after the wire's initial formation.

Based on the above TEM analysis, another phenomenon needs to be emphasized. While some magnetite nanowires grew along the $[111]_M$ and $<211>_M$ directions, we did not observe the ε-Fe$_2$O$_3$ phase in these structures. However, in all the examined Fe$_3$O$_4$ nanowires grown along the $[110]_M$ direction, without exception, we found the presence of the ε-Fe$_2$O$_3$ phase. It also should be noted that nanowires grown along the $<110>_M$ direction have the longest length (normally >2μm) compared to those found to grow along the $[111]_M$ and $<211>_M$ directions. Therefore, the fast-growth direction of Fe$_3$O$_4$ nanowires should be the $<110>_M$ direction. Possibly, the magnetite nanowires growing along the fast-growth $<110>_M$ direction provide sufficiently exposed surface for oxidation to the ε-Fe$_2$O$_3$ phase, while the nanowires growing along the $[111]_M$ and $<211>_M$ directions provide small surface area making it difficult for this transition to proceed. More work is needed to fully understand this phenomenon.

The SAED patterns in Figures 3b and 8d reveal the existence of 120° rotation domains. These can be seen more clearly in the bright-field and dark-field images shown in Figure 9a and b. Based on the contrast in Figure 9b, besides the 120° rotation domain boundaries (the interfaces between bright and
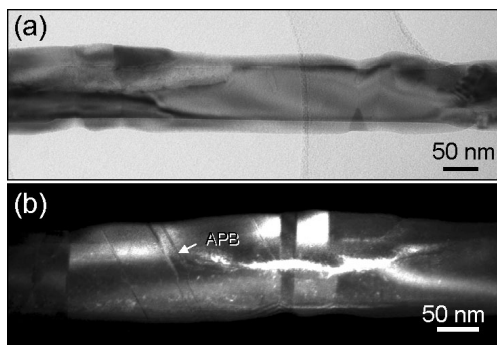
Figure 9. a) Bright-field and b) dark-field image to show the antiphase domain boundaries and 120° rotation domain walls in the ε-Fe₂O₃ phased nanowire.

dark domains), another type of planar defect, antiphase boundaries (APBs), also exist as the white arrowhead indicates.

The HRTEM image in Figure 10a shows three separated 120° domains. The FFTs of domains "D1"and "D2" are displayed in Figure 10b and c. After indexing the FFT patterns, the identified *b* axes of each domain have been marked in Fig-
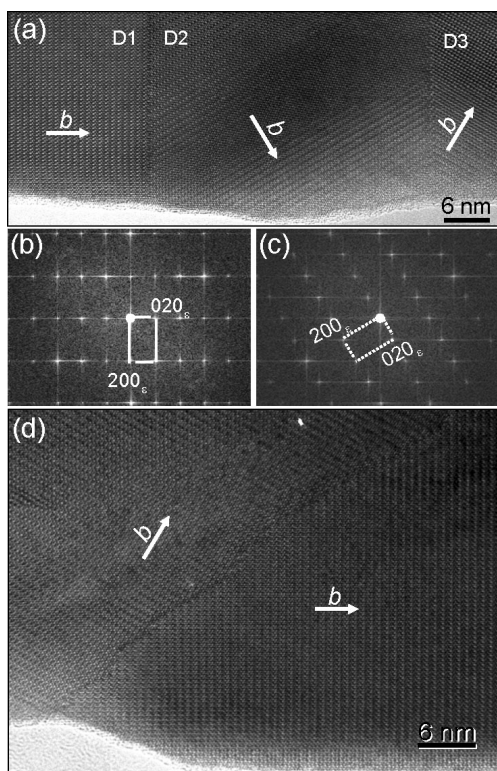

Figure 10. a,d) HRTEM images of the 120° rotation domains as shown in Figure 9. b,c) FFT of the domain D1 and D2 in (a).

ure 10a. The flat 120° rotation domain boundaries lie in (010) or (110) planes. Irregular domain boundaries were also observed, as shown in Figure 10d. The formation of these rotation domain boundaries is related simply to the redistribution of Fe ions in the oxygen interstitial sites from one domain to another. The stacking of the close-packed oxygen ions, which serve as

the framework of the structure, remains intact.[25,26] Therefore, the formation of the irregular-shaped domain boundaries is energetically reasonable.

The HRTEM image of an APB is shown in Figure 11. The boundary plane normally takes the (100) plane. The displacement across the defect is ca. 1/3 *b* ∼ 2.9 Å. Similar to the case of the 120° rotation domain walls, the framework of close-packed
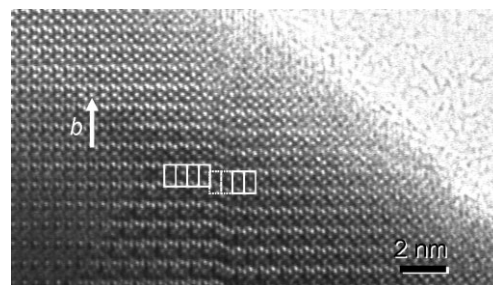
Figure 11. HRTEM image of a ε-Fe₂O₃ phase nanowire, showing the atomic scale structure of an antiphase domain boundary.

oxygen remains intact; only the Fe ions readjust positions across the defect. In such κ-alumina crystal structures, the displacement of the elementary APB corresponds to a cation shift of half the O–O distance along the *b* axis,[19] which is around 1.45 Å in the ε-Fe₂O₃ crystal. The observed APBs in Figure 11 can be considered as two elementary APBs combined together.

Considerable pure ε-Fe₂O₃ nanowires have been characterized by using our TEM works, such as the wire shown in Figures 9–11. From a statistic point of view, more than 50 % of the ε-Fe₂O₃ nanowires do not show the diffraction pattern of Fe₃O₄. It indicates that wires are fully oxidized into the ε-Fe₂O₃ phase. In other words, the yield of the ε-Fe₂O₃ phase nanowire is fairly high.

3. Conclusions

By using pulsed laser deposition (PLD) method and Fe₃O₄ powder as precursor, we synthesized not only one-dimensional Fe₃O₄ nanowires but also high-yield ε-Fe₂O₃ nanowires. The crystal structure of these nanowires and the structural relationship between magnetite and ε-Fe₂O₃ phases have been characterized by using a systematic TEM study. The pure magnetite nanowires were found to grow along the [111]$_M$ and <211>$_M$ directions. Nanowires that grew along the <110>$_M$ direction were found in every instance to contain the ε-Fe₂O₃ phase, with the fixed structural relationship of (001)$_{ε-Fe_2O_3}$ ∥ (111)$_{Fe_3O_4}$, [010]$_{ε-Fe_2O_3}$ ∥ <110>$_{Fe_3O_4}$. Remarkably, we found no indication of the existence of γ-Fe₂O₃ during the synthesis process. Therefore, the phase transition may be described as from magnetite to ε-Fe₂O₃, then to hematite, a novel structural evolution route in iron oxide. HRTEM images and electron diffraction enabled us to observe this entire structural transformation within a single nanowire. Also, the 120° rotation domain boundaries and antiphase boundaries in our ε-Fe₂O₃ nanowires have been

characterized. We believe this to be the first report of ε-Fe$_2$O$_3$ transition from magnetite, rather than the γ-Fe$_2$O$_3$ phase. The novel fabrication route reported here should provide researchers with another tool toward practical synthesis of the epsilon phase, a promising and exciting material for many future applications.

4. Experimental

The iron oxide nanowires were synthesized by using a PLD process, using a target of pressed magnetite powder as the source material. The detailed experimental setup has been published elsewhere [20]. The structural analysis was carried out using a JEOL 4000EX high-resolution transmission electron microscope operating at 400 kV. Electron diffraction patterns as well as high-resolution images of several nanostructures were recorded and developed on film. The HRTEM image simulations were performed using Cerius2 commercial software [27].

[1] L. A. Bursill, R. L. Withers, *J. Appl. Crystallogr.* **1979**, *12*, 287.
[2] G. A. Ferguson, Jr., M. Hass, *Phys. Rev.* **1958**, *112*, 1130.
[3] C. Greaves, *J. Solid State Chem.* **1983**, *49*, 325.
[4] M. Boudeulle, H. Batis-Landoulsi, C. Leclercq, P. Vergnon, *J. Solid State Chem.* **1983**, *48*, 21.
[5] Y. Watanabe, S. Takemura, Y. Kashiwaya, K. Ishii, *J. Phys. D: Appl. Phys.* **1996**, *29*, 8.
[6] H. Forestier, G. Guoit-Guillain, *C. R. Académie des Sciences.* **1934**, *199*, 720.
[7] E. Tronc, C. Chanéac, J. P. Jolivet, *J. Solid State Chem.* **1998**, *139*, 93.
[8] K. Kelm, W. Mader, *Z. Anorg. Allg. Chem.* **2005**, *631*, 2383.
[9] R. Zboril, M. Mashlan, K. Barcova, M. Vujtek, *Hyperfine Interact.* **2002**, *139/140*, 597.
[10] E. Tronc, C. Chanéac, J. P. Jolivet, J. M. Grenèche, *J. Appl. Phys.* **2005**, *98*, 053 901.
[11] J. Jin, K. Hashimoto, S. Ohkoshi, *J. Mater. Chem.* **2005**, *15*, 1067.
[12] S. Ohkoshi, S. Sakurai, J. Jin, K. Hashimoto, *J. Appl. Phys.* **2005**, *97*, 10K 312.
[13] R. M. Cornell, U. Schwertmann, *The Iron Oxides: Structure, Properties, Reactions, Occurrence and Uses*, VCH, Weinheim, Germany **1996**.
[14] A. Ito, M. Shinkai, H. Honda, T. Kobayashi, *J. Biosci. Bioeng.* **2005**, *100*, 1.
[15] H. Taguchi, *J. Phys. IV* **1997**, *7*, 299.
[16] V. Pillai, D. O. Shah, *J. Magn. Magn. Mater.* **1996**, *163*, 243.
[17] M. Gich, A. Roig, C. Frontera, E. Molins, J. Sort, M. Popovici, G. Chouteau, D. Martin y Marero, J. Nogues, *J. Appl. Phys.* **2005**, *98*, 044 307.
[18] M. Popovici, M. Gich, D. Niznansky, A. Roig, C. Savii, L. Casas, E. Molins, K. Zaveta, C. Enache, J. Sort, S. de Brion, G. Chouteau, J. Nogues, *Chem. Mater.* **2004**, *16*, 5542.
[19] M. Gich, C. Frontera, A. Roig, J. Fonteuberta, E. Molins, N. Bellido, C. Simon, C. Fleta, *Nanotechnology* **2006**, *17*, 687.
[20] J. R. Morber, Y. Ding, M. Haluska, Y. Li, J. P. Liu, Z. L. Wang, R. L. Snyder, *J. Phys. Chem. B* **2006**, *110*, 21 672.
[21] M. E. Fleet, *Acta Crystallogr.* **1981**, *37*, 917.
[22] R. L. Withers, L. A. Bursill, *J. Appl. Crystallogr.* **1980**, *13*, 346.
[23] R. S. Wagner, W. C. Ellis, *Appl. Phys. Lett.* **1964**, *4*, 89.
[24] JCPDS-39-1346, International centre for diffraction data (1999).
[25] P. Liu, J. Skogsmo, *Acta Crystallogr. Sect. B: Struct. Science* **1991**, *47*, 425.
[26] B. Ollivier, R. Retoux, P. Lacorre, D. Massiot, G. Férey, *J. Mater. Chem.* **1997**, *7*, 1049.
[27] J. M. Cowley, A. Moodie, *Acta Crystallogr.* **1957**, *10*, 609.